



## On the response of $Y_3Al_5O_{12}:Ce$ (YAG: Ce) powder scintillating screens to medical imaging X-rays

I. Kandarakis<sup>a,\*</sup>, D. Cavouras<sup>a</sup>, I. Sianoudis<sup>b</sup>, D. Nikolopoulos<sup>a,c</sup>,  
A. Episkopakis<sup>a</sup>, D. Linardatos<sup>a</sup>, D. Margetis<sup>a</sup>, E. Nirgianaki<sup>a</sup>, M. Roussou<sup>a</sup>,  
P. Melissaropoulos<sup>a</sup>, N. Kalivas<sup>d</sup>, I. Kalatzis<sup>a</sup>, K. Kourkoutas<sup>b</sup>,  
N. Dimitropoulos<sup>e</sup>, A. Louizi<sup>c</sup>, C. Nomicos<sup>f</sup>, G. Panayiotakis<sup>d</sup>

<sup>a</sup>Department of Medical Instruments Technology, Technological Educational Institution of Athens, Agion Spyridonos Street, Egaleo, Aigaleo, 122 10 Athens, Greece

<sup>b</sup>Department of Physics, Chemistry and Materials Technology, Technological Educational Institution of Athens, 122 10 Athens, Greece

<sup>c</sup>Laboratory of Medical Physics, University of Athens, Greece

<sup>d</sup>Laboratory of Medical Physics, University of Patras, Greece

<sup>e</sup>Department of Medical Imaging, "Euromedica" Medical Center, 2 Mesogeion Ave., Athens, Greece

<sup>f</sup>Department of Electronics, Technological Educational Institution of Athens, 122 10 Athens, Greece

Received 28 January 2004; received in revised form 27 July 2004; accepted 6 August 2004

Available online 16 September 2004

### Abstract

The aim of this study was to examine  $Y_3Al_5O_{12}:Ce$  (also known as YAG:Ce) powder scintillator under X-ray imaging conditions. This material shows a very fast scintillation decay time and it has never been used in X-ray medical imaging. In the present study various scintillator layers (screens) with coating thickness ranging from 13 to 166 mg/cm<sup>2</sup> were prepared in our laboratory by sedimentation of  $Y_3Al_5O_{12}:Ce$  powder. Optical emission spectra and light emission efficiency (spectrum area over X-ray exposure) of the layers were measured under X-ray excitation using X-ray tube voltages (80–120 kVp) often employed in general medical radiography and fluoroscopy. Spectral compatibility with various optical photon detectors (photodiodes, photocathodes, charge coupled devices, films) and intrinsic conversion efficiency values were determined using emission spectrum data. In addition, parameters related to X-ray detection, energy absorption efficiency and K-fluorescence characteristic emission were calculated. A theoretical model describing radiation and light transfer through scattering media was used to fit experimental data. Intrinsic conversion efficiency ( $\eta_C \approx 0.03–0.05$ ) and light attenuation coefficients ( $\sigma \approx 26.5$  cm<sup>2</sup>/g) were derived through this fitting.  $Y_3Al_5O_{12}:Ce$  showed peak emission in the wavelength range 530–550 nm. The light emission efficiency was found to be maximum for the 107 mg/cm<sup>2</sup> layer. Due to its "green" emission spectrum,  $Y_3Al_5O_{12}:Ce$  showed excellent compatibility (of the order

\*Corresponding author. Tel.: +30-10-5385-375; fax: +30-10-5910-975

E-mail address: [kandarakis@teiath.gr](mailto:kandarakis@teiath.gr) (I. Kandarakis).

of 0.9) with the sensitivity of many currently used photodetectors. Taking into account its very fast response  $\text{Y}_3\text{Al}_5\text{O}_{12}:\text{Ce}$  could be considered for application in X-ray imaging especially in various digital detectors.

© 2004 Published by Elsevier B.V.

PACS: 07.85; 78.65; 42.80

Keywords: Scintillators; Phosphor screens; Luminescence efficiency; Spectral compatibility; X-ray imaging

## 1. Introduction

Scintillators or phosphors are used as radiation to light converters in radiation detectors of a large variety of medical imaging applications (from conventional and digital X-ray radiography and X-ray computed tomography to positron tomography and portal imaging). Most radiation detectors consist of a scintillator/phosphor layer coupled to an optical detector (photographic emulsion film, photocathode, photodiode, etc.) [1–5]. Among the principal criteria to take into account in evaluating scintillators for X-ray medical imaging applications are: the X-ray quantum detection and absorption efficiency, the emission of K-characteristic radiation, the intrinsic radiation to light conversion efficiency, the light emission efficiency, the spectrum of the emitted light and the spectral compatibility to optical detectors incorporated in medical imaging detectors.

The aim of the present study was to investigate the response of  $\text{Y}_3\text{Al}_5\text{O}_{12}:\text{Ce}$  (also known as YAG:Ce) scintillator to X-rays employed in medical imaging. To follow the requirements of projection X-ray imaging (radiography, fluoroscopy)  $\text{Y}_3\text{Al}_5\text{O}_{12}:\text{Ce}$  was employed as powder (often referred to as P-46 phosphor) in the form of granular phosphor screens prepared in our laboratory.  $\text{Ce}^{3+}$  ion-doped scintillators are very attractive for medical imaging applications due to their very fast response. This has been attributed to the energy level scheme of the  $\text{Ce}^{3+}$  ion including a  $4f^1$  ground state configuration, containing one electron, and a  $5d^1$  excited state configuration split into five levels due to electric crystal field effects [6–8]. After excitation an allowed  $5d \rightarrow 4f$  radiative transition occurs, which is a mechanism for fast scintillation decay [6–9]. In addition

$\text{Y}_3\text{Al}_5\text{O}_{12}:\text{Ce}$  exhibits a bright light emission peaking in the green spectral region, attributed to strong crystal-field effects [6,10]. This property is of particular interest for X-ray imaging, since in modern digital and conventional X-ray imaging detectors, scintillators are often coupled to optical photon detectors (e.g., amorphous silicon photodiodes, ortho-chromatic films) exhibiting high sensitivity to green light. Some additional intrinsic properties of  $\text{Y}_3\text{Al}_5\text{O}_{12}:\text{Ce}$  scintillator that may be of interest for medical imaging applications are as follows: (1) its volume density ( $\rho = 4.15 \text{ g/cm}^3$ ), which is comparable to that of other scintillators already in use (e.g., CsI, NaI,  $\text{Y}_2\text{O}_2\text{S}$ ,  $\text{La}_2\text{O}_2\text{S}$ , etc.), (2) its effective atomic number ( $Z_{\text{eff}} = 23.8$ ) and its radiation detection index  $\rho Z_{\text{eff}}^4$  ( $\rho Z_{\text{eff}}^4 = 1.33 \times 10^4$ ), which are rather low as compared to those of the aforementioned scintillators, (3) its energy band gap ( $E_G = 7.01 \text{ eV}$ ) between the valence and the conduction bands, which determines the energy required to create electron–hole pairs and affects the intrinsic conversion efficiency of the phosphor material [1,4–7,11], (4) its K-fluorescence yield ( $\omega_K = 0.67$ ) [12], determining the probability of K-characteristic fluorescence X-ray production. This radiation may either escape the scintillator, thus reducing the absorbed radiation energy, or it may be reabsorbed in scintillator and cause image blurring, (5) its refractive index (1.83) affecting the intrinsic optical properties of the scintillator [13] as well as the fraction of light collected by the optical detector.

In this study, the optical emission spectrum and the light emission efficiency (LE) of the  $\text{Y}_3\text{Al}_5\text{O}_{12}:\text{Ce}$  powder scintillator were determined under conditions used in X-ray imaging (medical radiography and fluoroscopy). Measurements were performed in a medical radiography unit

emitting polychromatic X-rays from a tungsten target tube. X-ray tube voltage varied between 40 and 140 kVp. Scintillator layers with coating thickness from 16 to 166 mg/cm<sup>2</sup>, covering most X-ray imaging applications, were prepared. In addition the optical spectra were employed to calculate the spectral compatibility of Y<sub>3</sub>Al<sub>5</sub>O<sub>15</sub>:Ce with the spectral sensitivity of various optical photon detectors used in X-ray imaging systems. In addition data concerning: the quantum detection efficiency (QDE), the energy absorption efficiency (EAE), the total absorption efficiency (TAE), the probability of K-characteristic radiation emission and re-absorption, the intrinsic X-ray to light conversion efficiency (absorbed X-ray energy converted into light within scintillator) and the intrinsic quantum conversion gain (number of light photons generated within scintillator per absorbed X-ray) were calculated.

Y<sub>3</sub>Al<sub>5</sub>O<sub>12</sub>:Ce, in single-crystal or in ceramic form, has been previously studied using X-rays,  $\gamma$ -rays, cathode-rays and  $\alpha$ -particles for various non-medical radiation detection applications [14]. High light yields (14000–17500 photons/MeV) have been reported when Y<sub>3</sub>Al<sub>5</sub>O<sub>12</sub>:Ce is excited by  $\gamma$ -rays or other forms of ionizing radiation [15]. Powder Y<sub>3</sub>Al<sub>5</sub>O<sub>12</sub>:Ce has also been evaluated in the form of granular screens under UV and low energy (22–50 kV) X-ray excitation for non-medical applications, e.g., in detectors in fusion devices [16]. It has also been used for phosphor conversion of light-emitting diodes and in single-crystal TV screens for electron microscopes [17]. To our knowledge the Y<sub>3</sub>Al<sub>5</sub>O<sub>12</sub>:Ce powder scintillator has not been previously studied for X-ray medical imaging applications (i.e., under poly energetic X-rays excitation employed in X-ray medical radiography, fluoroscopy and computed tomography).

## 2. Materials and methods

### 2.1. Theory and definitions

#### 2.1.1. Optical emission spectrum and light emission efficiency

In the present study, we have performed optical emission spectrum measurements under X-ray

excitation. Based on these data the light emission efficiency was determined by the following relation:

$$\eta_{\lambda} = \left( \int \psi_{\lambda}(\lambda, V) d\lambda \right) X^{-1} \quad (1)$$

where  $\psi_{\lambda}(\lambda, V)$  is the spectral distribution of the emitted light energy fluence (optical emission spectrum),  $X$  is the X-ray exposure associated with the incident X-ray beam,  $\lambda$  denotes light wavelength,  $V$  is the X-ray tube voltage. The integral in relation (1) is evaluated over the emission spectrum wavelength range and expresses spectrum area and hence the total emitted light intensity.

Light emission efficiency was also theoretically evaluated in terms of intrinsic scintillator properties by the Hamaker–Ludwig theoretical model [18] (see appendix for details)

$$\langle \eta_{\lambda} \rangle_E = \int \psi_0(E) \eta_e(E) \eta_C g_{\lambda}(\sigma, \beta, \rho_n) \times dE / \int \psi_0(E) dE \quad (2)$$

where  $\eta_C$  is the intrinsic conversion efficiency,  $\eta_e$  is the X-ray energy absorption efficiency and  $g_{\lambda}(\sigma, \beta, \rho_n)$  is a function describing the light transmission efficiency (LTE) of the scintillator. LTE expresses the light attenuation effects (scattering and absorption), within a granular scintillator layer [18,19].  $\sigma$  is the reciprocal light diffusion length [19].  $\beta$  is an optical parameter related to the reflectivity of a scintillator layer of infinite thickness [18]. Both  $\sigma$  and  $\beta$  are optical attenuation coefficients related to the light scattering ( $s$ ) and to the light absorption coefficient ( $a$ ) (see appendix).  $\rho_n$  is the light reflectivity at scintillator surfaces [18]. In relation (2),  $\eta_{\lambda}$  is averaged over the spectrum  $\psi_0(E)$  of incident X-ray energy fluence. The X-ray spectrum was determined following the TASMIP model [20,21]. For mono-energetic radiation, relation (2) is simplified to the product,  $\eta_{\lambda} = \eta_e \eta_C g_{\lambda}$ .

$\sigma$  and  $\beta$  have been shown to be of importance for X-ray imaging detectors, since they express light spread effects within granular scintillators. These effects degrade image quality, e.g., spatial resolution and signal-to-noise ( $S/N$ ) ratio. To

provide an estimation of image quality, a previously developed theoretical model [22], taking into account the value of  $\sigma$ , was used to predict image quality parameters, namely: (i) the modulation transfer function (MTF), expressing image contrast and spatial resolution and (ii) the detective quantum efficiency (DQE), expressing image  $S/N$  ratio transfer efficiency [22–25].

### 2.1.2. Radiation detection

The efficiency of a scintillator to detect photons is described by the quantum detection efficiency (QDE). QDE is the fraction of incident photons interacting with the scintillator [20]. For poly energetic X-rays the QDE of a scintillator layer of coating thickness  $w$  is written as

$$\langle \eta_q \rangle_E = \frac{\int_0^{E_0} \phi_0(E)(1 - e^{-(\mu_{\text{tot},t}(E)/\rho)w})dE}{\int_0^{E_0} \phi_0(E)dE}. \quad (3)$$

$\phi_0(E)$  is the X-ray photon fluence (photons per unit of area) incident on the scintillator. The spectrum of  $\phi_0(E)$  may be given in terms of the X-ray energy fluence spectrum ( $\psi_0 = \phi_0 E$  [19,20]).  $\mu_{\text{tot},t}(E)/\rho$  is the X-ray total mass attenuation coefficient of the scintillator [26,27]. X-ray imaging detectors are energy integrating systems, i.e., their output signal is proportional to the X-ray energy absorbed within the scintillator. Hence, when evaluating X-ray imaging systems, the calculation of the energy absorption efficiency (EAE) is also of importance [20]. EAE may be calculated by the relation

$$\langle \eta_e \rangle_E = \frac{\int_0^{E_0} \psi_0(E)dE \left( \frac{\mu_{\text{tot},en}(E)}{\mu_{\text{tot},t}(E)} \right) (1 - e^{-(\mu_{\text{tot},t}(E)/\rho)w})dE}{\int_0^{E_0} \psi_0(E)dE}. \quad (4)$$

$\psi_0$  is the incident X-ray energy fluence and  $\mu_{\text{tot},en}$  is the total mass energy absorption coefficient of the scintillator.  $\mu_{\text{tot},en}$  includes all mechanisms of energy deposition locally at the point of X-ray interaction within the scintillator's mass. All secondary photons, e.g., K-characteristic fluorescence X-rays, created just after the primary interaction effect, are assumed to be lost [12,26–28]. Thus EAE, being a measure of the locally absorbed energy, represents more accu-

rately the efficiency of a detector to capture the useful X-ray imaging signal (i.e., the spatial distribution of primary X-ray absorption events). Attenuation and absorption coefficients were calculated using tabulated data [12,26].

### 2.1.3. Generation of K-fluorescence characteristic radiation

When the incident X-ray photon energy just exceeds the energy of the K-shell for photoelectric absorption, radiation absorption increases suddenly. However, a fraction of the absorbed X-ray energy may be re-remitted in the form of K-fluorescence characteristic X-rays. K-fluorescence photons may either be re-absorbed, away from the point of primary interaction, or escape the scintillator. Since X-ray imaging detectors must precisely register the spatial distribution of the highest possible amount of incident radiation energy, both re-absorption and escape of K-fluorescence photons degrade detector performance and image quality. The effects of K-fluorescence radiation may be important in the energy range employed in X-ray imaging.

To examine the K-fluorescence effect on detector performance the scintillator was assumed to be divided into a large number ( $I$ ) of elementary thin layers of thickness  $\Delta w$ . The probability,  $p_{Fy}^i$ , of generating a K-fluorescence photon in the  $i$ th layer of the scintillator, after the incidence of a radiation photon of energy  $E$ , may be written as follows [29,30]:

$$p_{Fy}^i(E, E_y) = \frac{w_z [\mu_P(Z, E)/\rho]}{[\mu_T(E)/\rho]} f_K \omega_K I_y \eta_q(E, \Delta w_i). \quad (5)$$

The index  $y$  stands either for a  $K_\alpha$  or a  $K_\beta$  X-ray fluorescent photon.  $w_z$  is the fractional weight of yttrium, the highest atomic number ( $Z$ ) element in the scintillator, exhibiting higher probability for photoelectric interaction.  $[\mu_P(Z, E)/\rho]$  is the total mass photoelectric X-ray attenuation coefficient of yttrium at energy  $E$ .  $[\mu_T(E)/\rho]$  is the total X-ray mass attenuation coefficient of the scintillator material ( $Y_3Al_5O_{12}$ : Ce) at energy  $E$ .  $f_K$  is a factor expressing the relative contribution of the K-shell photoelectric cross section ( $\tau_K$ ) to the total

photoelectric effect cross section  $\tau$  ( $f_K = \tau_K/\tau$ ).  $\omega_K$  is the K-fluorescence yield of yttrium, being the ratio of the averaged number of K-fluorescence X-rays produced over the number of vacancies created in the K-shell (i.e., excluding the probability of Auger electron production).  $I_y$  is the relative frequency of either  $K_\alpha$  or  $K_\beta$  fluorescence X-ray photon production [27]. The ratio containing the photon interaction coefficients and the fractional weight, in Eq. (5), expresses the probability for photoelectric interaction in yttrium. If this is multiplied by parameters  $\omega_K$ ,  $f_K$  and  $I_y$ , then the probability of K-fluorescence photon production per absorbed primary X-ray is obtained.  $\eta_q(E, \Delta w_i)$  represents the attenuation of incident radiation within the  $i$ th layer (see appendix for details). Then the probability,  $p_{F_y}^w$ , of generating a K-characteristic fluorescence photon within the whole scintillator per incident primary X-ray photon, may be calculated by the sum

$$p_{F_y}^w(E_y, E) = \sum_{i=1}^I p_{F_y}^i(E, E_y). \quad (6)$$

The probability of a K-fluorescence X-ray photon, generated at the  $i$ th scintillator layer, emitted within a solid-angle element  $\Delta\Omega_j$ , and interacting at another layer within the scintillator, e.g., the  $e$ th layer (see Ref. [30] for detailed explanation), may be written as

$$p_{A_j}^{i,e}(E_y, \Delta\Omega_j) = \frac{\Delta\Omega_j}{4\pi} \eta_q(E_y, \Delta w_{e-i}) \quad (7)$$

where  $\eta_q(E_y, \Delta w_{e-i})$  expresses the interaction of K-fluorescence photons, emitted from the  $i$ th layer within the  $e$ th layer (see appendix).

The probability of generation and re-absorption of a K-characteristic fluorescence photon, within the whole scintillator, is obtained after summation over all the elementary thin layers  $i$  and  $e$  and over the solid angle elements  $j$ , as follows

$$p_{A,F}^w(E, E) = \sum_{i=1}^I p_{F_y}^i(E, E_y) \sum_{e=1}^I \sum_{j=1}^J p_{A_j}^{i,e}(E_y, \Delta\Omega_j). \quad (8)$$

To simulate medical X-ray imaging conditions, where poly energetic X-ray beams are used, relations (6) and (8) were averaged over the

X-ray spectrum.

$$\langle p_{A,F}^w \rangle_E = \int \phi_0(E) p_{A,F}^w(E) dE / \int \phi_0(E) dE. \quad (9)$$

X-ray spectrum was expressed in terms of quantum fluence since  $p_{A,F}^w$  is defined as probability per incident photon.

#### 2.1.4. Intrinsic conversion efficiency

The intrinsic conversion efficiency  $\eta_C$  (fraction of absorbed radiation energy that is converted into light within the scintillator mass) [17] has been expressed as follows [6,11]:

$$\eta_C = (\hbar\bar{\omega}/\beta_0 E_G) S Q \quad (10)$$

where  $\hbar\bar{\omega}$  is the average energy of emitted light photons.  $\beta_0 E_G$  represents the average energy that must be transferred by a fast electron (e.g. a photoelectron) to create an electron–hole pair in the scintillator.  $E_G$  is the forbidden energy band gap between the valence and the conduction energy bands of the scintillator material [6,11,31].  $\beta_0$  is a parameter related to energy losses to lattice vibrations. For  $Y_3Al_5O_{12}$  scintillator,  $\beta_0 = 5.6$  [5,10].  $S$  is the electron–hole pair energy transfer efficiency expressing the fraction of electron–hole pair energy transferred to the luminescent centre (LC).  $Q$  is the quantum efficiency of LC, expressing the fraction of  $S$  absorbed at LC.

The intrinsic conversion efficiency corresponds to a number  $m_0$  of light photons generated per X-ray detected within scintillator's mass. This number may be defined as the intrinsic quantum conversion gain of the scintillator and may be calculated by the relation

$$m_0 = (\eta_C E / \hbar\omega) = (E / \beta_0 E_G) S Q. \quad (11)$$

$E$  denoting the energy of an X-ray quantum. For polychromatic X-ray beams  $m_0$  must be averaged over the detected X-ray spectrum.

$$\langle m_0 \rangle_E = \int \phi_0(E) \eta_q(E) m_0(E) \times dE / \int \phi_0(E) \eta_q(E) dE. \quad (12)$$

### 2.1.5. Spectral compatibility to optical detectors

The suitability of a scintillator–optical detector combination is estimated by the spectral compatibility between the optical emission spectrum  $\psi(\lambda)$  of the scintillator and the spectral sensitivity  $S_{\text{OD}}(\lambda)$  of the optical detector. This compatibility is expressed by the spectral matching factor ( $c_s$ ) defined as follows

$$c_s = \int \psi_N(\lambda) S_{\text{NOD}}(\lambda) d\lambda / \int S_{\text{NOD}}(\lambda) d\lambda \quad (13)$$

where  $\psi_N$  and  $S_{\text{NOD}}$  are the normalised scintillator emission spectrum and the normalised optical detector spectral sensitivity given as follows

$$\psi_N(\lambda) = \psi(\lambda) / \psi_{\text{max}} \quad S_{\text{NOD}}(\lambda) = S_{\text{OD}}(\lambda) / S_{\text{ODmax}}$$

$\psi_{\text{max}}$  and  $S_{\text{ODmax}}$  are the peak values of  $\psi(\lambda)$  and  $S_{\text{OD}}(\lambda)$ .

## 2.2. Measurements and calculations

The scintillator material, employed in this study, was in phosphor powder form supplied by Phosphor Technology Ltd. (code: QMK58/N-C1). The density of this material was 4.15 g/ml and the particle size distribution had a mean value of 6.6  $\mu\text{m}$ . The material was used in the form of layers (scintillating screens) prepared in our laboratory by sedimentation of the phosphor powder on fused silica substrates (spectrosil B).  $\text{Na}_2\text{SiO}_3$  was used as binding material between the powder particles. The coating thickness of the layers were 12.6, 33, 42, 62.97, 107.44 and 166.47  $\text{mg}/\text{cm}^2$ . The layers were irradiated using a Philips Optimus medical X-ray radiography unit. Various X-ray tube voltages were employed, ranging from 40 to 140 kVp. During X-ray excitation, the scintillator optical emission spectrum was measured by Ocean Optics S2000 grating spectrometer incorporating a CCD sensor (Ocean Optics Inc). Scintillator's light was transferred to the sensor through an optical fibre (Avantes FCB-UV 400-2). This spectrometer was calibrated using a series of prototype LED light sources (Kingbright Co.) ranging from 400 nm to 640 nm. The incident X-ray exposure was measured with a Radcal 2026C ionisation chamber-based dosimeter (chamber code: 20  $\times$  6-3). X-ray energy and X-ray

photon fluence,  $\psi_0$  and  $\phi_0$ , respectively, were determined from exposure ( $X$ ) measurements using the appropriate conversion factor ( $\psi_0 = [X / (\mu_{\text{en}} / \rho)_{\text{air}}] e / W_{\text{air}}$  and  $\phi_0 = \psi_0 / E$ ) [32].

Light emission efficiency experimental data were fitted by the Hamaker–Ludwig model equation (relation (2)). Fitting was performed employing the Trust–Region fitting algorithm incorporated in the non-linear fitting toolbox of Matlab\_v6.5 [MathWorks\_Inc, MA, USA]. Parameters  $\eta_C$ ,  $\sigma$  and  $\beta$  were allowed to vary within suitably selected intervals (see results and discussion section). To provide an estimation of the imaging performance of  $\text{Y}_3\text{Al}_5\text{O}_{12}:\text{Ce}$  screens, the final values of  $\eta_C$ ,  $\sigma$  and  $\beta$  were used as input data to a theoretical model [19,24], which was employed to calculate MTF and DQE (see appendix).

QDE and EAE, were calculated using corresponding formulas (3) and (4). The intrinsic conversion gain, the intrinsic conversion efficiency and the spectral matching factor were determined according to formulas (10)–(13) using measured emission spectrum data. Spectral sensitivity curves corresponding to various well-known optical photon detectors used with medical imaging systems were employed in formula (13) for matching factor determination.

## 3. Results and discussion

The optical emission spectra measured at 100 kVp for various scintillator coating thicknesses are presented in Fig. 1. Spectra measured at lower or higher X-ray tube voltages were of similar shape but of different intensity. Depending on scintillator thickness and on X-ray tube voltage, maximum spectral values were found within the spectral range from 532 to 555 nm. Each spectrum covered a wide spectral range from approximately 480 nm to about 700 nm, i.e., extending from the blue-green into the orange-red spectral region. These spectra are similar or close to those obtained in previous studies [15,16] using different types of exciting radiation (gamma rays, UV, etc.).  $\text{Y}_3\text{Al}_5\text{O}_{12}:\text{Ce}$  emission spectra depict the  $\text{Ce}^{3+}$  ion characteristic emission within the particular  $\text{Y}_3\text{Al}_5\text{O}_{12}$  host lattice, which, due to crystal field

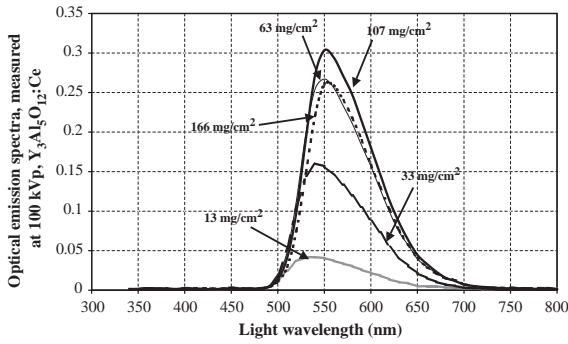


Fig. 1. Optical emission spectra of  $Y_3Al_5O_{12}:Ce$  measured at 100 kVp for various scintillator coating thicknesses.

effects, removes the spectrum towards the green region [6,9–11,15,33]. As shown in Fig. 1, the emission spectrum area, expressing emitted light intensity, increases with increasing scintillator thickness up to the  $107 \text{ mg/cm}^2$  layer. The  $166 \text{ mg/cm}^2$  layer spectrum had lower intensity than both the  $107$  and  $63 \text{ mg/cm}^2$  layers. Differences in spectral area, as well as some slight differences in shape, among the spectra of the layers could be discussed on the basis of (i) increased X-ray absorption in thick layers, resulting in increased light generation within the scintillator's mass and (ii) filtering effects and spectrum shape distortion caused by the significant light scattering and light absorption phenomena within the granular structure of powder scintillator layers. These effects are more important in thick scintillators. This may explain the relatively decreased emission of the  $166 \text{ mg/cm}^2$  layer. Another aspect to observe in Fig. 1 is the slight spectrum peak shift towards longer wavelengths as layer thickness increases. This may be clearly seen if the  $166 \text{ mg/cm}^2$  layer spectrum is compared to that of the  $63 \text{ mg/cm}^2$  layer. Such spectral alterations could be attributed to the inverse wavelength dependence of light scattering and absorption effects, which may be responsible for the relative attenuation of the low wavelength portion in the  $166 \text{ mg/cm}^2$  layer spectrum.

Fig. 2 shows the variation of experimental and theoretical LE with scintillator coating thickness determined at 100 kVp. Experimental LE data, plotted as points in the diagram, were determined

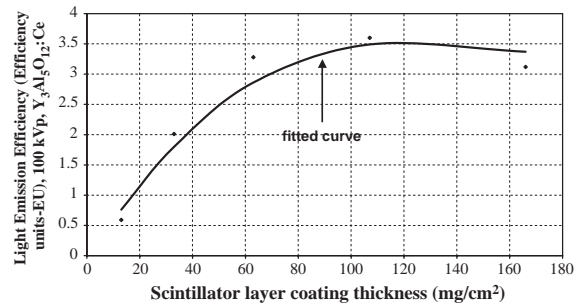


Fig. 2. Variation of experimental and theoretical light emission efficiency with scintillator coating thickness determined at 100 kVp. Efficiency units:  $\mu\text{W} \times \text{m}^{-2}/(\text{mR} \times \text{s}^{-1})$ .

according to relation (1) using optical emission spectrum and X-ray exposure measurements. Theoretical data, shown as solid line, correspond to best-fitted curve, calculated by relation (2). The scintillator layer of  $107 \text{ mg/cm}^2$  exhibited maximum experimental emission efficiency. This maximum was also observed at all X-ray voltages. The corresponding theoretical data (solid line) indicate that maximum emission efficiency may be obtained in a range of coating thicknesses from approximately  $105$  to  $125 \text{ mg/cm}^2$ . The experimental light emission efficiency of the  $166 \text{ mg/cm}^2$  layer was 20–30% lower than that of the  $107 \text{ mg/cm}^2$  layer. This reduction was previously qualitatively explained (Fig. 1). However, a quantitative explanation could be given in terms of the function  $g_\lambda(\sigma, \beta, \rho_n)$  in relation (2) (see appendix). Fitting of relation (2) was performed by allowing the fitting parameters to vary within suitably predetermined intervals, i.e. the values of the intrinsic conversion efficiency were allowed to vary within a minimum of  $\eta_C = 0.0139$ , previously found under UV excitation measurements [16], and a maximum of  $\eta_C = 0.055$ , calculated by relation (10) assuming  $S = Q = 1$ . The light attenuation coefficient  $\sigma$  was selected first by assuming that light attenuation (scattering and absorption) is affected by light wavelength [13,34,35]. Second, previously found data on powder scintillators with emission spectra peaking in the  $530$ – $550 \text{ nm}$  range were taken into account (e.g.,  $\sigma = 26$ – $34 \text{ cm}^2/\text{g}$  for  $Gd_2O_3:S:Tb$ ,  $\sigma = 30 \text{ cm}^2/\text{g}$  for  $La_2O_3:S:Tb$ ,  $\sigma = 28$ – $30 \text{ cm}^2/\text{g}$  for  $Y_2O_3:S:Tb$ ,  $\sigma = 33.4 \text{ cm}^2/\text{g}$  for  $ZnSCdS:Ag$ , etc.)

[22–25].  $\sigma$  was then allowed to vary from 25 to  $35 \text{ cm}^2/\text{g}$ .  $\beta$  was allowed to vary around 0.03 which is a value found in previous studies for most scintillator materials [16,24,25]. Different values were found for  $\eta_C$ . Depending on X-ray tube voltage,  $\eta_C$  ranged from 0.0276 to 0.0463. The corresponding values of  $\sigma$  varied slowly around  $26.5 \text{ cm}^2/\text{g}$  while  $\beta$  was in all cases equal to 0.03. The final values of parameter  $\sigma$  were somewhat lower than those found for the aforementioned green emitting powder scintillators [22–25]. This difference may be explained by considering that  $\text{Y}_3\text{Al}_5\text{O}_{12}:\text{Ce}$  emission spectrum (Fig. 1) exhibits a tail penetrating in the red spectral region by up to 700 nm. Taking into account that light attenuation is inversely proportional to light wavelength, the presence of this long wavelength part of the spectrum could explain the relative decrease of light attenuation coefficient  $\sigma$ .

Parameters  $\eta_C$ ,  $\sigma$  and  $\beta$  were additionally employed for theoretical determination of MTF and DQE curves (see relations (A.2.1) and (A.2.2) in appendix) [24]. Examples of such data are plotted in Figs. 3a and b, respectively. MTF, which is related to light spread effects within granular scintillators and expresses spatial resolution, was found to decrease rapidly between the 13 and  $63 \text{ mg}/\text{cm}^2$  layers. MTF differences among thicker layers were found to be very small. DQE, expressing image  $S/N$  ratio, was found to be higher for thick layers in the low spatial frequency range. This may be explained by considering that in the low spatial frequency range, DQE is principally affected by the emitted light fluence ( $\phi_\lambda$  in relation (A.2.2) in appendix), which usually increases with thickness (see Fig. 1), while low frequency MTF (in numerator of (A.2.2)) is very close to unity for all scintillator layers. As spatial frequency increases, the DQE of thin layers shows a tendency to decrease at a slower rate, principally due to the superiority of the corresponding MTF. To obtain a validation of the aforementioned theoretical calculations an experimental MTF curve is provided in Fig. 3a. This curve was obtained by experimental methods described in previous studies [36]. A  $\text{Y}_3\text{Al}_5\text{O}_{12}:\text{Ce}$  scintillating screen ( $33 \text{ mg}/\text{cm}^2$ ) was brought in close contact with a piece of radiographic film (Agfa Ortho CP-G

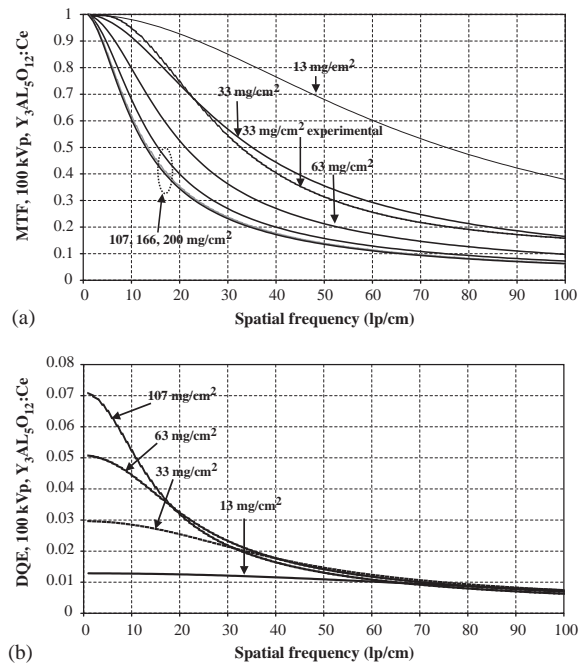


Fig. 3. (a) MTF curves of  $\text{Y}_3\text{Al}_5\text{O}_{12}:\text{Ce}$  for various scintillator screens at 100 kVp. (b) Calculated DQE curves of  $\text{Y}_3\text{Al}_5\text{O}_{12}:\text{Ce}$  for various scintillator screens at 100 kVp.

plus). An MTF test pattern (Nuclear Associates, typ-53) was placed in front of the screen. The pattern-screen-film system was then exposed to 100 kVp X-rays and a digital pattern image was obtained after film chemical processing and film image digitisation (Agfa Duoscan). The MTF curve was finally determined by suitable processing of digital data as described in previous studies [24,25]. The experimental curve was found close to the corresponding theoretical curve, being approximately 3.5% higher at  $10 \text{ mm}^{-1}$  and approximately 10% lower at  $40 \text{ mm}^{-1}$ . The two curves cross at  $23 \text{ mm}^{-1}$ .

Shown in Fig. 4 is the variation of calculated QDE and EAE with X-ray tube voltage for the  $107 \text{ mg}/\text{cm}^2$  scintillator layer. Calculations were performed for a range of X-ray tube voltages wider than that available in ordinary medical radiographic units. This was achieved in order to estimate scintillator detection efficiency under medical examinations requiring specialised equipment (e.g., breast and some type of chest

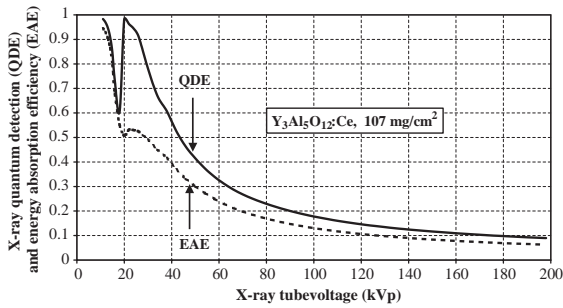


Fig. 4. Variation of calculated QDE and EAE of  $Y_3Al_5O_{12}:Ce$  with X-ray tube voltage for the  $107\text{ mg/cm}^2$  scintillator layer.

examinations). The first point to note is that EAE differs significantly from QDE. As it may be seen, at  $40\text{ kVp}$ , EAE (0.394) is approximately 30% lower than QDE (0.568). This deviation decreases with increasing X-ray tube voltage, being approximately 26% at  $100\text{ kVp}$ . The differences between EAE and QDE show that only a fraction of the total amount of radiation energy detected is locally imparted (EAE). Hence, only this fraction contributes to accurate spatial registration of photons and accurate image formation. In the low X-ray tube voltage region from  $25$  to  $30\text{ kVp}$ , QDE takes values higher than  $0.8$ . In the same region EAE ranges from  $0.53$  to  $0.49$ . For higher voltages employed in general radiography and fluoroscopy QDE retains values higher than  $0.4$  for voltages up to  $50\text{ kVp}$ . To compare the X-ray absorption performance of  $Y_3Al_5O_{12}:Ce$  with currently employed materials, similar calculations were performed for  $Gd_2O_2S$  and  $CsI$  scintillators, which are widely used in medical radiography, fluoroscopy and X-ray computed tomography. Calculations have shown that in the  $30$ – $40\text{ kVp}$  voltage range, the EAE of  $Y_3Al_5O_{12}:Ce$  is very close to that of  $CsI$  (e.g.,  $0.38$  and  $0.4$  at  $40\text{ kVp}$ , respectively) however, it is clearly lower than that of  $Gd_2O_2S$  ( $0.5$  at  $40\text{ kVp}$ ). At higher voltages both  $Gd_2O_2S$  and  $CsI$  had higher energy absorption efficiency than  $Y_3Al_5O_{12}:Ce$ . These findings were expected, considering the lower value of the radiation detection index  $pZ_{eff}^4$  ( $=1.33 \times 10^6$ ) of  $Y_3Al_5O_{12}:Ce$  with respect to corresponding index values of  $Gd_2O_2S$  and  $CsI$  ( $103 \times 10^6$ – $38 \times 10^6$ , respectively).

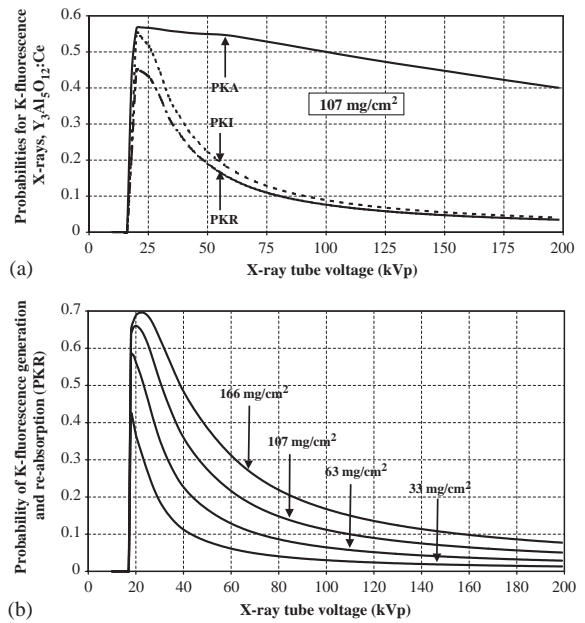


Fig. 5. (a) Variation of probabilities PKI (probability of K-fluorescence X-ray photon generation per incident X-ray), PKA (probability of K-fluorescence X-ray photon generation per absorbed X-ray), and PKR (probability of generation and re-absorption of a K-fluorescence X-ray per incident X-ray) with X-ray tube voltage for the  $107\text{ mg/cm}^2$  scintillator layer. (b) Variation of PKR of  $Y_3Al_5O_{12}:Ce$  with X-ray tube voltage for various scintillator screens at  $100\text{ kVp}$ .

Fig. 5a illustrates the variation of probabilities related to K-fluorescence X-ray production with tube voltage. Shown in the figure are the following: (i) the probability of K-fluorescence X-ray photon generation per incident X-ray (PKI), where  $PKI \equiv p_F^w$  (relations (6) and (A.3.2) in appendix), (ii) the probability of K-fluorescence X-ray photon generation per absorbed X-ray (PKA), where  $PKA = w_Z [[\mu_P(Z, E)/\rho]/[\mu_T(E)/\rho]] \omega_K f_K I_Y$  and (iii). The probability of generation and re-absorption of a K-fluorescence X-ray per incident X-ray (PKR), where  $PKR \equiv p_{A,F}^w$  (relations (8) and (A.3.4) in appendix). Data shown in Fig. 5a correspond to the  $107\text{ mg/cm}^2$  layer. The values for the photoelectric mass attenuation coefficient  $\mu_P$  and the relative contribution of the K-shell to the photoelectric effect  $f_K$  ( $0.856$ ) of yttrium were taken from Storm and Israel [27], the fluorescence yield  $\omega_K$  of yttrium ( $\omega_K = 0.67$ ) was taken from Hubbel

et al. [11]. To simplify the calculations we have considered that only one K-fluorescence photon was created with energy equal to the weighted average of the energies of the  $K_{\alpha}$ ,  $K_{\beta}$  photons. Hence, the relative frequency  $I_y$  of either  $K_{\alpha}$  or  $K_{\beta}$  fluorescence photon emission was taken  $I_y = 1$ . PKI, PKA and PKR showed peak values at approximately 20 kVp. This value is numerically slightly higher than the energy of the K-absorption edge of Yttrium at 17 keV. This shift is due to the poly energetic nature of X-rays. PKA decreases slowly with X-ray tube voltage, varying from 0.565 at 20 kVp to 0.40 at 200 kVp. PKA is a function of intrinsic scintillator material properties, some of which ( $\mu_P$ ,  $\mu_T$ ) depend on incident X-ray energy while others ( $w_Z$ ,  $\omega_K$ ,  $f_K$ ,  $I$ ) are independent. Hence this variation of PKA reflects the decrease of the ratio  $[\mu_P(Z, E)/\rho]/[\mu_T(E)/\rho]$  expressing the relative probability of photoelectric effect in the corresponding energy range. In contrast PKI and PKR decrease more rapidly with X-ray voltage, e.g., from 0.55 to 0.04 for PKI, and from 0.45 to 0.034 for PKR, within the range from 20 to 200 kVp. This is because PKI and PKR, expressed by relations (6) and (8) respectively, depend, in addition, on the probability of incident X-ray interaction within the scintillator ( $\eta_q$  in relation (5)). This probability also decreases with X-ray energy. As shown in Fig. 5a, the amount of K-fluorescence characteristic radiation reabsorbed within the scintillator (PKR values) may be a significant fraction of the total K-radiation generated (PKI). Since K-fluorescence photons are randomly re-absorbed within the scintillator, high PKR values indicate degradation in the accuracy of incident photons spatial registration and consequently degradation in image quality. This effect is more pronounced in thick scintillator layers as shown in Fig. 5b, which shows PKR for various coating thicknesses. Therefore, PKR is an extra factor, which, in addition to light spread effects (see Fig. 3a for MTF), degrades spatial resolution in thick scintillator layers. Finally, it must be noted that PKR effects are of relatively lower importance for X-ray tube voltages higher than 80–100 kVp which are often used in general radiography and computed tomography.

Fig. 6a depicts the variation of the intrinsic quantum conversion gain (light photons created within scintillator per interacting X-ray photon) with X-ray tube voltage. The curves were calculated according to relations (11) and (12) using  $S = Q = 1$ ,  $E_G = 7.01$  eV and  $\beta_0 = 5.6$  [6,11]. Within the range from 40 to 140 kVp,  $m_0$  increases from approximately 900 to 1600 light photons per interacting X-ray. These data represent the net intensification effect of radiographic scintillating screens, which however depends on incident X-ray energy (relation 11). Data in Fig. 6b show curves determined by relation (10), for various scintillator layers. The average light photon energy  $h\bar{\omega}$ , in the denominator of (10), was found by the relation  $h\bar{\omega} = hc/\bar{\lambda} = hc/(\int \psi(\lambda)\lambda d\lambda / \int \psi(\lambda) d\lambda)$ ,  $\bar{\lambda}$  being the mean wavelength of the emitted light. Relation (10) provides the intrinsic conversion efficiency, however, the data shown in Fig. 6b do not represent strictly this efficiency. This is because the average energy  $h\bar{\omega}$  was found from measured optical emission spectra ( $\psi(\lambda)$ ), which, due to light attenuation effects, are slightly distorted with

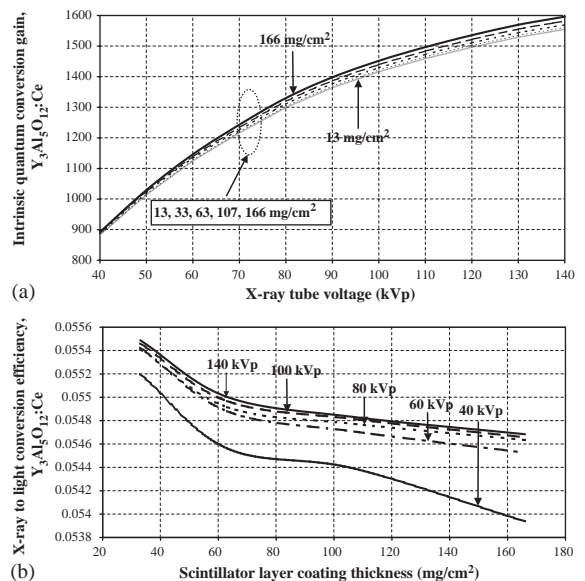


Fig. 6. (a) Variation of intrinsic quantum conversion gain (light photons created within scintillator per interacting X-ray photon) of  $Y_3Al_5O_{12}:Ce$  with X-ray tube voltage for various scintillator screens. (b) X-ray to light conversion efficiency of  $Y_3Al_5O_{12}:Ce$ .

respect to emission spectra generated within the scintillator material. This distortion can also be assessed from discrepancies observed among the measured optical spectra (in Fig. 1) corresponding to various scintillator layers. To estimate a good approximation to true intrinsic conversion efficiency, only data corresponding to insignificant light attenuation effects (i.e. light transmission efficiency close to unity) should be taken into account. This may be accomplished when thin scintillator layers and deeply penetrating X-rays, i.e., high X-ray tube voltages, are used. Following these considerations the value  $\eta_C$  (Calculated) = 0.05549 corresponding to 33 mg/cm<sup>2</sup> layer at 140 kVp was selected. It should be mentioned that this value of  $\eta_C$ , is higher than those found by fitting relation (2) to experimental light emission efficiency data (0.0276–0.0463). This is so because data in Fig. 6b represent maximum intrinsic conversion efficiency values (i.e., assuming  $S=Q=1$ ). Contrasting the Y<sub>3</sub>Al<sub>5</sub>O<sub>12</sub>:Ce intrinsic conversion efficiency to that of other scintillators, it is found comparable or slightly higher to values that have been reported for conventional CaWO<sub>4</sub> radiographic screens (0.035–0.05) [9,11,20]. However it is lower than the intrinsic conversion efficiency of most rare earth powder scintillators, examined in previous studies: e.g., 0.20 for Gd<sub>2</sub>O<sub>2</sub>S:Tb, 0.18 for La<sub>2</sub>O<sub>2</sub>S:Tb, 0.11 for Y<sub>2</sub>O<sub>2</sub>S:Eu, 0.095 for Y<sub>2</sub>O<sub>3</sub>:Eu, etc. [22–25]. This difference is due to (i) the large values of the forbidden energy band gap ( $E_G=7.1$  eV) between valence and conduction bands of Y<sub>3</sub>Al<sub>5</sub>O<sub>12</sub>:Ce and (ii) the

high value of parameter  $\beta_0(=5.6)$ , attributed to Y<sub>3</sub>Al<sub>5</sub>O<sub>12</sub>:Ce [6,11].

The difference between fitted and calculated  $\eta_C$  may provide an indication of the actual values of the product  $SQ$  (transfer and quantum efficiency related to the electron–hole transfer to luminescent centres).  $SQ$  could be estimated by the ratio:  $\eta_C$  (fitted)/ $\eta_C$  (calculated) =  $SQ$ , where  $\eta_C$  (calculated) represents the intrinsic conversion efficiency determined by relation (10). To estimate  $SQ$ , the aforementioned value of  $\eta_C$  (calculated) = 0.05549 corresponding to high light transmission efficiency, i.e., corresponding to the thin layer of 33 mg/cm<sup>2</sup> with easier light transmission, at high X-ray tube voltages (140 kVp) is appropriate. Thus, taking into account that  $\eta_C$  (fitted) was also found to change with X-ray tube voltage, various values of  $SQ$  were estimated with approximate mean value  $SQ=0.79$ . Since  $Q$  is most often taken to be equal to unity [7], we may consider  $S \approx 0.79$ .

The spectral matching factors of Y<sub>3</sub>Al<sub>5</sub>O<sub>12</sub>:Ce emission spectrum with various optical photon detectors, calculated by relation (13), are listed in Table 1. Emission spectrum data for Gd<sub>2</sub>O<sub>2</sub>S:Tb were taken from previous studies [24]. The spectrum of CsI:Tl was taken from tabulated data [37]. Data concerning Gd<sub>2</sub>O<sub>2</sub>S:Tb and CsI:Tl scintillators are also shown for comparison. Fig. 7 shows spectral sensitivity curves of various optical photon detectors [38–40]. The optical detectors listed are those most frequently used in various imaging applications [1–5], namely: (i) Amorphous hydrogenated silicon photodiode

Table 1  
Matching factors of YAG:Ce, CsI:Tl and Gd<sub>2</sub>O<sub>2</sub>S:Tb with optical detectors

Optical detectors	Scintillators		
	YAG:Ce	CsI:Tl	Gd <sub>2</sub> O <sub>2</sub> S:Tb
a-Si:H (I04 H)	0.886084	0.777818	0.917869
a-Si:H (I08 H)	0.936751	0.840115	0.937118
c-Si (S1227-BR HAMAMATSU)	0.853321	0.814455	0.792252
c-Si (S1337-BR HAMAMATSU)	0.601128	0.568782	0.550159
c-Si (S1133 HAMAMATSU)	0.888157	0.812706	0.913567
CCD (S100AF SITE <sup>®</sup> )	0.783689	0.693474	0.675272
CCD (S100AB SITE <sup>®</sup> )	0.950683	0.935825	0.927695
GaAsP (HAMAMATSU)	0.913044	0.807302	0.868114
AGFA Ortho CP-G Plus	0.494019	0.434927	0.645419

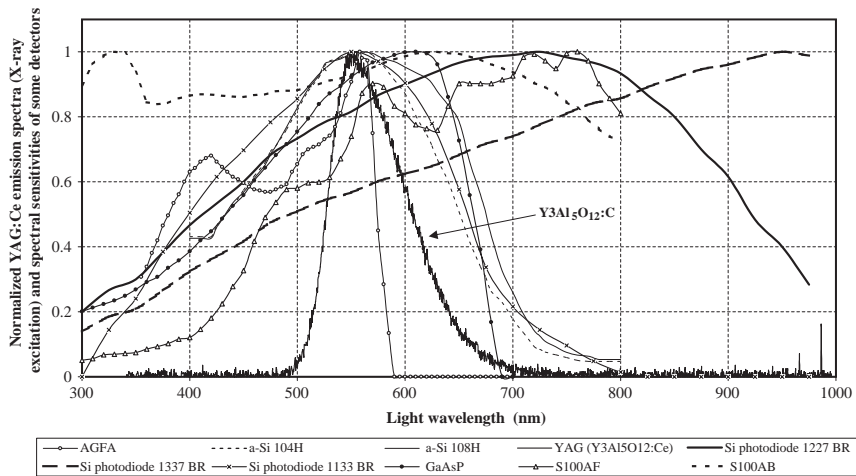


Fig. 7.  $Y_3Al_5O_{12}:Ce$  optical emission spectrum with spectral sensitivity curves of various optical photon detectors.

(a-Si:H), employed in photodiodes and thin film transistors of modern active matrix flat panel detectors used in X-ray digital radiography, fluoroscopy, mammography as well as in some X-ray computed tomography detectors. Spectral sensitivities of two a-Si:H are shown corresponding to photodiodes differing in their intrinsic layer thickness (800 and 400 nm, respectively). Both matching factors were found to be very high (0.936 and 0.886). These values are higher than those of CsI and equal to one of the values corresponding to  $Gd_2O_2S:Tb$ . (ii) Crystalline silicon (c-Si) based photodiodes used in various detectors (X-ray-computed tomography,  $\gamma$ -ray cameras for single-photon emission tomography). Very high matching factor values (0.888, 0.853) were also obtained, in this case, which are higher than most of the values corresponding to CsI:Tl and  $Gd_2O_2S:Tb$ . (iii) CCD sensor arrays used in digital radiography and digital mammography systems as well as in many non-medical imaging applications. The values obtained were 0.783 and 0.950 which are also higher than those of CsI:Tl and  $Gd_2O_2S:Tb$ . (iv) GaAsP photocathode incorporated in various types of image intensifiers and in photomultipliers (0.91). (v) Orthochromatic film used with radiographic cassettes in conventional X-ray radiography (0.49). All these data indicate that  $Y_3Al_5O_{12}:Ce$  scintillator may be efficiently coupled to all practical types of optical photon detectors

and hence it may be used in a variety of applications especially those requiring digital imaging detectors.

#### 4. Summary and conclusion

In the present study,  $Y_3Al_5O_{12}:Ce$  powder scintillator layers with various thicknesses were prepared and were examined under X-ray imaging conditions. Peak light emission efficiency was exhibited for the  $107\text{ mg/cm}^2$  layer. The X-ray quantum detection efficiency and X-ray energy absorption efficiency were found adequate for detection of X-rays used in medical radiology, although the value of the radiation detection index  $\rho Z_{\text{eff}}^4$  is lower than that of some currently used materials. The intrinsic conversion efficiency (0.03–0.055) was found to be slightly higher than that of conventional radiographic screens, however, it was clearly lower than the corresponding values of rare earth scintillators. The emission spectrum of  $Y_3Al_5O_{12}:Ce$  powder scintillator was found to peak around 530–550 nm and showed excellent spectral compatibility with currently used optical photon detectors. Taking into account its very fast response, this scintillator could be considered for applications in X-ray imaging especially in digital imaging systems.

## Acknowledgement

This work was financially supported by the research programme EPEAEK “Archimidis”.

## Appendix

### A.1. Theoretical model for Light emission efficiency

According to this model, incident X-rays and light photons, generated within scintillator mass, propagate along a direction vertical to the scintillator’s surface. X-ray absorption, light generation and attenuation are incorporated in a differential equation describing light emission by an elementary thin scintillator layer  $dw$  within the screen, as follows [18]:

$$\frac{d\psi_{\lambda f}}{dw} = \frac{1}{2}\eta_C\mu\psi_0 \exp(-\mu w) - (a+s)\psi_{\lambda f} + s\psi_{\lambda b}. \quad (\text{A.1.1})$$

Eq. (A.1.1) expresses the light intensity  $d\psi_{\lambda f}$  per unit of length, produced within an elementary thin layer  $dw$ , which is directed towards the back scintillator side. The first term in the right-hand side of Eq. (A.1.1) gives the fraction of absorbed X-ray energy (i.e.,  $\mu\psi \exp(-\mu w)$ ) that is converted into light.  $\eta_C$  is the intrinsic X-ray to light conversion efficiency.  $\psi_0$  is the X-ray energy flux incident on the thin layer  $dw$ .  $\mu$  is the X-ray energy absorption coefficient. The factor  $\frac{1}{2}$  is applied to express that only half of the produced light is directed towards the back scintillator’s side [18].  $\psi_{\lambda f}$  is the forward propagating light intensity,  $\psi_{\lambda b}$  is the backwards propagating light intensity.  $a$  and  $s$  are the light absorption and light scattering coefficients.  $s\psi_{\lambda b}$  in Eq. (A.1.1) is the fraction of backwards directed light, which is back-scattered and thus re-directed towards the forward direction. The solution of Eq. (A.1.1), based on the Hamaker–Ludwig theory [18], provides the theoretical expression for light

emission efficiency ( $\eta_\lambda$ ) as follows:

$$\eta_\lambda = \frac{\psi_\lambda}{\psi_0} = \frac{\eta_C\eta_\varepsilon(1-\rho_0)}{(\mu^2-\sigma^2)} \times \frac{(\mu-\sigma)(\rho_1-\beta)e^{-\sigma w} + 2(\sigma+\mu\beta)e^{-\mu w} - (\mu+\sigma)(\rho_1-\beta)e^{-\sigma w}}{(\rho_1+\beta)(\rho_0+\beta)e^{-\sigma w} - (\rho_1-\beta)(\rho_0-\beta)e^{-\sigma w}}. \quad (\text{A.1.2})$$

$\psi_\lambda$  is the light energy fluence emitted by the scintillator determined experimentally,  $\psi_0$  was determined from X-ray exposure measurements (X) [32],  $\eta_\varepsilon$  is the energy absorption efficiency,  $\sigma$  is the light attenuation coefficient of the phosphor given in terms of the optical scattering ( $s$ ) and the optical absorption ( $a$ ) coefficients ( $\sigma = [a(a+2s)]^{1/2}$ ). Since layer thickness  $w$  is expressed in units of  $\text{mg}/\text{cm}^2$ , coefficients  $a$ ,  $s$  and  $\sigma$  are given in units of  $\text{cm}^2/\text{g}$ .  $\rho_0$ ,  $\rho_1$  are optical parameters expressing light reflectivity at front and back scintillator surfaces, defined as:  $\rho_n = (1-r_n)/(1+r_n)$ , with  $n=0,1$ .  $r_n$  is the optical reflection coefficients at the front ( $n=0$ ) and back ( $n=1$ ) scintillator surfaces [18].  $\rho_n$  is a unitless quantity.  $\beta$  is an optical parameter which had originally defined as a reflectivity parameter:  $\beta = (1-r_\infty)/(1+r_\infty)$ ,  $r_\infty$  being the reflection coefficient corresponding to a very thick layer with negligible light transmission through it [18].  $\beta$  has been also expressed in terms of  $a$  and  $s$  [18]:  $\beta = [a/(a+2s)]^{1/2}$ . According to both relations  $\beta$  is a unitless quantity. Data on  $\rho_n$  were taken from previous studies [18,22–24]. Relation (A.1.2) was fitted to the experimental LE measurements using a Trust–Region algorithm. Best fit was obtained for specific values of parameters  $\eta_C$ ,  $\sigma$ ,  $\beta$  given in text.

### A.2. Theoretical model for MTF and DQE calculation

MTF and DQE were calculated by a model based on the theory of Swank [19], which has been published in a previous study [24]. MTF ( $M(v)$ ) was expressed as follows:

$$M(v) = \frac{\phi_\lambda(v)}{\phi_\lambda(0)} \quad (\text{A.2.1})$$

where  $\phi_\lambda(v)$  is the emitted light photon fluence expressed in the spatial frequency domain (Fourier space) as a function of  $\sigma$  and  $\beta$  by a relation similar to (A.1.2) [19,24], obtained by converting energy

fluence into photon fluence [24]. In this relation parameter  $\sigma$  was replaced by the spatial frequency ( $v$ ) dependent function  $(\sigma^2 + 4\pi^2 v^2)^{1/2}$  [19,24], where  $v$  is expressed in units of  $\text{cm}^2/\text{g}$ , similar to  $\sigma$ . DQE is defined as  $(\text{SNR}_{\text{output}}/\text{SNR}_{\text{input}})^2$ , SNR denoting the  $S/N$  ratio in an imaging system. In the case of scintillating screens DQE may be expressed as follows [24]:

$$\text{DQE} = \frac{[\phi_\lambda M(v)]^2}{\phi_0 W(v)} \quad (\text{A.2.2})$$

where  $W(v)$  is the noise power spectrum (NPS), expressing image quantum and structure noise in the spatial frequency domain.  $W(v)$  may be also given in terms of  $\sigma$  and  $\beta$  [23–25,41].

In the model used for MTF and DQE calculation, it was assumed that the output signal of a scintillating screen, i.e., the emitted light photon fluence  $\phi_\lambda$ , is expressed in terms of mean values of random variables ( $\phi_0, \eta_q, m_0, g_\lambda$ , see Section 2 for details) e.g.,  $\phi_\lambda$  expresses the mean number of emitted light photons per unit of screen area,  $m_0$  is the mean number of light photons created within the scintillator mass per X-ray absorbed etc. Accordingly quantum noise and noise power spectrum are expressed in terms of the variances of  $\phi_0, \eta_q, m_0, g_\lambda$ , [5,19,23,41,42]. At zero-frequency, DQE reduces to a simple relation incorporating the so-called Swank factor or statistical factor [5,12,23,43–46]. This factor is given by the ratio  $M_1^2/M_2$ , where  $M_1, M_2$  are the first and second moments of the emitted light pulses statistical distribution, a light pulse being the number ( $m_0 g_\lambda$ ) of light photons emitted per X-ray photon absorbed. These moments correspond to the mean value (signal) and the variance (noise) respectively. Hence, the Swank factor may be thought of as a measure of the zero-frequency output  $S/N$  ratio of a scintillating screen. Finally, it should be noted that all model equations ((from A.1.1) to (A.2.2)) based either on the Hamaker–Ludwig theory or the Swank theory, ignore secondary electron range effects. At diagnostic X-ray energies, this range is of the order of 10–30  $\mu\text{m}$  [5] and its effect on image quality may be considered of minor importance.

### A.3. Theoretical model for generation and absorption of K-fluorescence X-rays

The scintillator was assumed to be divided into a large number ( $I$ ) of elementary thin layers of thickness  $\Delta\omega$ . The probability,  $p_{Fy}^i$ , of generating a K-fluorescence photon in the  $i$ th layer of the scintillator, after the incidence of a radiation photon of energy  $E$ , may be written as follows [29,30]:

$$p_{Fy}^i(E, E_y) = \frac{w_Z [\mu_P(Z, E)/\rho]}{[\mu_T(E)/\rho]} f_K \omega_K I_y \times \left\{ \exp\left[-\frac{\mu_T(E)}{\rho}(i-1)\Delta\omega\right] - \exp\left[-\frac{\mu_T(E)}{\rho}i\Delta\omega\right] \right\}. \quad (\text{A.3.1})$$

The index  $y$  stands either for a  $K_\alpha$  or  $K_\beta$  X-ray fluorescent photon.  $w_Z$  is the fractional weight of yttrium, the higher atomic number ( $Z$ ) element in the scintillator, exhibiting higher probability for photoelectric interaction.  $[\mu_P(Z, E)/\rho]$  is the total mass photoelectric X-ray attenuation coefficient, at energy  $E$ , for yttrium.  $[\mu_T(E)/\rho]$  is the total X-ray mass attenuation coefficient of the scintillator material ( $\text{Y}_3\text{Al}_5\text{O}_{12}$ ; Ce) at energy  $E$ .  $f_K$  is a factor expressing the relative contribution of the K-shell photoelectric cross section ( $\tau_K$ ) to the total photoelectric effect cross section  $\tau(f_K = \tau_K/\tau)$ .  $\omega_K$  is the K-fluorescence yield of yttrium, being the ratio of the averaged number of K-fluorescence X-rays produced over the number of vacancies created in the K-shell (i.e., excluding the probability of Auger electron production).  $I_y$  (taken to be =1) [29–30,41] is the relative frequency of either  $K_\alpha$  or  $K_\beta$  fluorescence X-ray photon production [27,29,30]. The first factor in Eq. (A.3.1), i.e., the ratio containing the photon interaction coefficients and the fractional weight expresses the probability for photoelectric interaction with the high  $Z$  element (yttrium). If this is multiplied by parameters  $\omega_K, f_K$  and  $I_y$  then the probability of K-fluorescence photon production per absorbed primary X-ray is obtained. The factor in curly brackets gives the attenuation of incident radiation within the  $i$ th layer. Then the probability,  $p_{Fy}^w$ , of generating a K-characteristic fluorescence photon within the whole scintillator per incident primary

X-ray photon may be calculated by the sum

$$p_{F_y}^w(E_y, E) = \sum_{i=1}^I p_{F_y}^i(E, E_y). \quad (\text{A.3.2.})$$

The probability of a K-fluorescence X-ray photon, generated at the  $i$ th scintillator layer, emitted within a solid-angle element  $\Delta\Omega_j$ , and interacting at the  $e$ th layer, may be written as

$$p_{A_j}^{i,e}(E_y, \Delta\Omega_j) = \frac{\Delta\Omega_j}{4\pi} \times \left\{ \exp \left[ -\frac{[\mu_T(E_y)/\rho](e-i-1)\rho\Delta w}{|\cos(j-1/2)\Delta\xi|} \right] - \exp \left[ -\frac{[\mu_T(E_y)/\rho](e-i)\rho\Delta w}{|\cos(j-1/2)\Delta\xi|} \right] \right\}. \quad (\text{A.3.3})$$

where  $\Delta\Omega_j$  is the solid angle element subtended at the point of K-characteristic X-ray fluorescence emission.  $\Delta\xi_j$  is the polar angle element corresponding to the solid angle element  $\Delta\Omega_j$ . The factor in curly brackets in Eq. (A.3.3) expresses the interaction of K-fluorescence photons within the  $e$ th layer [29–30,41].

The probability of generation and absorption of a K-characteristic fluorescence photon, within the whole scintillator, is obtained after summation over all the elementary thin layers  $i$  and  $e$  and over the solid angle elements  $j$ , as follows:

$$p_{A,F}^w(E_y, E) = \sum_{i=1}^I p_{F_y}^i(E, E_y) \sum_{e=1}^I \sum_{j=1}^J p_{A_j}^{i,e}(E_y, \Delta\Omega_j). \quad (\text{A.3.4})$$

## References

- [1] H. Wiczorek, *Radiat. Meas.* 33 (2001) 541.
- [2] E. Hell, W. Knüpfer, D. Mattern, *Nucl. Instr. and Meth. Phys. Res. A* 454 (2000) 40.
- [3] H.J. Besch, *Nucl. Instr. and Meth. Phys. Res. A* 419 (1998) 201.
- [4] C.W.E. van Eijk, *Phys. Med. Biol.* 47 (2002) R85.
- [5] J.A. Rowlands, Flat Panel Detectors for Digital Radiography, in: J. Beutel, H.L. Kundel, R.L. Van Metter (Eds.), *Handbook of Medical Imaging*, Vol. 1, Physics and Psychophysics, SPIE Press, Bellingham, 2000, pp. 234–248.
- [6] G. Blasse, B.C. Grabmaier, *Luminescent Materials*, Springer, Berlin, Heidelberg, 1994, p. 85.
- [7] C.W.E. van Eijk, *Nucl. Instr. and Meth. Phys. Res. A* 460 (2001) 1.
- [8] M. Grinberg, A. Sikorska, S. Kaczmarek, *J. Alloy. Comp.* 300–301 (2000) 158.
- [9] T. Kano, Principal phosphor materials and their optical properties, in: S. Shionoya, W.M. Yen (Eds.), *Phosphor Handbook*, CRC Press, Boca Raton, 1999, pp. 177–186.
- [10] E. Zych, C. Brecher, *J. Alloy. Comp.* 300–301 (2000) 495.
- [11] G. Blasse, *J. Lumin.* 60&61 (1994) 930.
- [12] J.H. Hubbel, P.N. Trehan, N. Singh, B. Chand, D. Mehta, M.L. Garg, R.R. Garg, S. Singh, S. Puri, *J. Phys. Chem. Ref. Data.* 23 (2) (1994) 339.
- [13] H.C. van de Hulst, *Light Scattering by Small Particles*, Wiley, New York, 1957, pp. 103–107.
- [14] T. Ludziejewski, M. Moszynski, M. Kapusta, D. Wolski, W. Klamra, K. Moszynska, *Nucl. Instr. and Meth. Phys. Res. A* 398 (1997) 287.
- [15] E. Zych, C. Brecher, J. Glodo, *J. Phys. Condens. Matter.* 12 (2000) 1947.
- [16] A. Baciero, L. Placentino, K.J. Mc Carthy, L.R. Barquero, A. Ibarra, B. Zurro, *J. Appl. Phys.* 85 (9) (1999) 6790.
- [17] R. Mueller-Mach, G.O. Mueller, M.R. Kramers, T. Trottier, *IEEE J. Sel. Top. Quant. Electron.* 8 (2) (2002) 339.
- [18] G.W. Ludwig, *J. Electrochem. Soc.* 118 (7) (1971) 1152.
- [19] R.K. Swank, *Appl. Opt.* 12 (8) (1973) 1865.
- [20] J.M. Boone, X-ray production, interaction, and detection in diagnostic imaging, in: J. Beutel, H.L. Kundel, R.L. Van Metter (Eds.), *Handbook of Medical Imaging*, Vol. 1, Physics and Psychophysics, SPIE Press, Bellingham, 2000, p. 40.
- [21] J.M. Boone, J.A. Seibert, *Med. Phys.* 24 (1997) 1661.
- [22] I. Kandarakis, D. Cavouras, *Nucl. Instr. and Meth. Phys. Res. A* 460 (2001) 412.
- [23] I. Kandarakis, D. Cavouras, G.S. Panayiotakis, C.D. Nomicos, *Phys. Med. Biol.* 42 (1997) 1351.
- [24] I. Kandarakis, D. Cavouras, C.D. Nomicos, G.S. Panayiotakis, *Nucl. Instr. and Meth. Phys. Res. B* 179 (2001) 215.
- [25] I. Kandarakis, D. Cavouras, *Eur. Radiol.* 11 (2001) 1083.
- [26] J.H. Hubbel, S.M. Seltzer, *Tables of X-ray mass attenuation coefficients and mass energy absorption coefficients 1 keV to 20 MeV for elements Z = 1 to 92 and 48 additional substances of dosimetric interest*. US Department of commerce. NISTIR 5632, 1995.
- [27] E. Storm, H. Israel, *Photon cross-sections from 0.001 to 100 MeV for elements 1 through 100*, Report LA-3753, Los Alamos Scientific Laboratory of the University of California, 1967.
- [28] J.H. Hubbel, *Phys. Med. Biol.* 44 (1999) R1–R22.
- [29] H.P. Chan, K. Doi, *Phys. Med. Biol.* 28 (5) (1983) 565.
- [30] I. Kandarakis, D. Cavouras, E. Ventouras, C. Nomicos, *Radiat. Phys. Chem.* 66 (2003) 257.
- [31] R. Alig, S. Bloom, *J. Electrochem. Soc.* 124 (7) (1977) 1136.
- [32] J.R. Greening, *Fundamentals of Radiation Dosimetry*, Institute of Physics, London, 1985, p. 56.

- [33] E. Zych, C. Brecher, A.J. Wojtowicz, H. Lingertat, *J. Lumin.* 75 (1997) 193.
- [34] R. Morlotti, *J. Photogr. Sci.* 23 (1975) 181.
- [35] C.F. Bohren, D.R. Huffman, *Absorption and Scattering of Light by Small Particles*, Wiley, New York, 1983 pp 28–136.
- [36] ICRU Repport 41, *Modulation transfer functions of screen-film systems*, 1986.
- [37] A.L.N. Stevels, *Medicamundi* 20 (1975) 12.
- [38] H. Aguas, E. Fortunato, V. Silva, L. Pereira, R. Martins, *Thin Solid Films* 403–404 (2002) 26.
- [39] Hamamatsu photodiode technical information, <http://www.hamamatsu.com>.
- [40] SITE data sheet: charged-coupled device family, <http://www.site-inc.com>.
- [41] N. Kalivas, E. Costaridou, I. Kandarakis, D. Cavouras, C.D. Nomicos, G.S. Panayiotakis, *Nucl. Instr. and Meth. Phys. Res. A* 490 (2002) 614.
- [42] R. Shaw, R. Van Metter, *Proc. SPIE* 454 (1984) 128.
- [43] M. Drangova, J.A. Rowlands, *Med. Phys.* 13 (1986) 150.
- [44] A. Ginzburg, C.E. Dick, *Med. Phys.* 20 (1993) 1013.
- [45] R. Nishikawa, M. Yaffe, *Med. Phys* 17 (1990) 894.
- [46] R. Van Metter, M. Rabbani, *Med. Phys.* 17 (1990) 65.